Sensors and Actuators A 148 (2008) 462–471

Contents lists available at ScienceDirect

Sensors and Actuators A: Physical

journal homepage: www.elsevier.com/locate/sna

Online methods to measure breaking force of bonding wire using a CMOS stress sensor and a proximity sensor

Aashish Shah*, Jaesik Lee, Michael Mayer, Y. Norman Zhou

Microjoining Laboratory, Department of Mechanical and Mechatronics Engineering, University of Waterloo, 200 University Avenue W. Waterloo, ON N2L3G1, Canada

ARTICLE INFO

Article history:
Received 13 August 2007
Received in revised form 2 September 2008
Accepted 3 September 2008
Available online 12 September 2008

Keywords:
Wire bonding
Thermosonic
Microsensor
Proximity sensor
Piezoresistive
Tail breaking force
Heat-affected zone

ABSTRACT

Two real-time, in situ methods to measure the breaking force of fine bonding wires while on the wire bonder are reported and compared. The first method uses a special test chip with a piezoresistive microsensor integrated next to the bonding pad. A 25 μm diameter Au wire piece is attached with a ball bond to the test pad of the microsensor. The wire piece between the ball bond and the lower edge of the wire clamps is 15 mm in length. The clamps tear the wire at a speed of 2 mm/s. The wire breaks at the heat-affected zone (HAZ) next to the ball bond. The microsensor is calibrated using FE models. The numerical results show that the microsensor signal is highly sensitive to ball and pad geometry, values of the piezoresistive coefficients, and the *z*-location of the microsensor under the bonding pad. This results in a high estimated error of about 46% for the calibration factor of the microsensor.

The second method uses a proximity sensor attached to the wire clamp of the bonding machine for which an accurate calibration is available. The proximity sensor is calibrated by hanging a weight of 22.2 g to the wire clamp. The average breaking force at the HAZ is measured to be 98.6 ± 1.67 mN. This value is approximately 77% of the breaking load of the non-heat affected wire as measured with a standard tensile tester. Using the proximity sensor method, an accurate calibration of the microsensor is found. The signal precisions of the microsensor and the proximity sensor are found to be approximately 1%. These methods are ideally suited for the automatic measurement of tail breaking force (TBF) as observed in thermosonic wire bonding processes.

1. Introduction

Among all variants of the wire bonding technologies, thermosonic gold wire bonding is the most widely used method in microelectronic packaging industry for establishing electrical interconnection between the internal circuitry of the semiconductor chip and the external leads of the package. It is estimated that more than 95% of semiconductor chips are ultrasonically connected with wire bonds [1]. The main reasons for the widespread use of wire bonding can be attributed to the nature of this process: self-cleaning, low temperature, high yield rate, low cost, and flexibility. However, due to the growing demands of the microelectronics industry, notably miniaturization, thinner wires, cost reduction, and higher yield, there is a constant need for improvements in this process.

In thermosonic gold ball bonding, a normal bonding force is utilized simultaneously with thermal and ultrasonic energy to form the ball bond (first bond) on the chip followed by the crescent or stitch bond (second bond) on the lead frames or the substrate. An important part of the bonding process is the formation of the wire tail on the second bond needed to form the free air ball (FAB) for the next ball bond. Before the wire tail can be formed by breaking the wire, it must be bonded to the substrate with sufficient strength that can withstand the high tensile force applied during wire breaking. It is reported that during the formation of the crescent bond, the wire is pinched by the capillary and a tail bond forms inside the inner chamfer of the capillary [2].

An unstable tail bond results in two bonding issues: tail lift-off or tail length variation. A tail lift-off or short tail results due to a tail bond that is not strong enough to hold the wire until the clamp closes to tear the wire off. This causes production stops because of the wire being blown out of the capillary, which has to be re-threaded manually by the operator. This reduces the mean time between assists (MTBA). Tail length variations are caused by non-optimized tail bond strength and can result in non-uniform formation of free air balls which are either too small or too big [3]. This is because a constant quantity of wire tail below the capillary is required to melt into a free air ball of consistent diameter. The force required for breaking the tail is an indicator of the quality and

* Corresponding author. Tel.: +1 519 888 4567x33326; fax: +1 519 885 5862.
E-mail address: ashah011@engmail.uwaterloo.ca (A. Shah).

0924-4247/$ – see front matter © 2008 Elsevier B.V. All rights reserved.
doi:10.1016/j.sna.2008.09.008

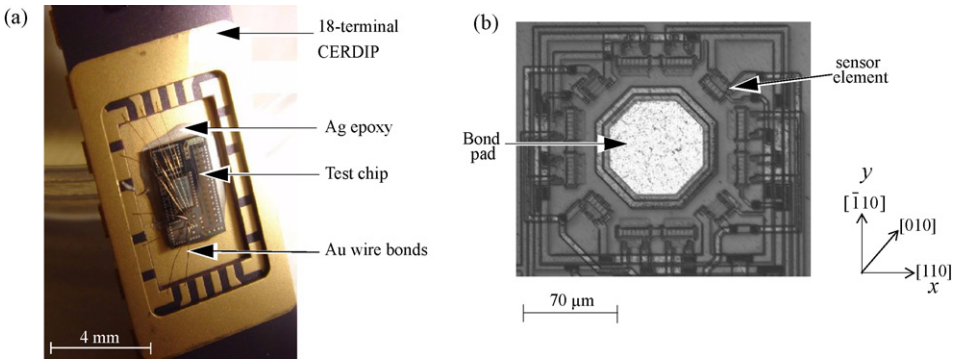

Fig. 1. (a) Photograph of bonded microsensor chip-package assembly. (b) Optical micrograph of microsensor bond pad with piezoresistors integrated adjacent to it.

strength of the tail bond. This tail pull strength is also called tail breaking force (TBF).

To further improve the TBF performance of advanced processes, new technologies to monitor TBF could be helpful to obtain an improved understanding of the tail bond mechanisms. This paper presents two online methods to measure the wire breaking force on the wire bonder using a microsensor and a proximity sensor. The microsensor method is studied using an FE simulation. The second method uses the proximity sensor mounted on the wire clamp of the bonding machine. Once calibrated, the proximity sensor method is used to measure and optimize the TBF process with novel wires [4,5].

2. Experimental details

A fully automatic ESEC 3100 wire bonder, manufactured by Oerlikon Esec, Cham, Switzerland, is used for the experiments. Advanced software options are provided by the wire bonder manufacturer, particularly recording the force sensed by the standard proximity sensor during the bonding operation. The wire material used is 99.99% pure standard gold wire, 25 μm (1 mil) in diameter, and manufactured by MK Electron, Yongin, South Korea. The capillary used is manufactured by a leading supplier and has a tip diameter of 100 μm, and chamfer diameter of 51 μm. A microsensor test chip specially designed by the Microjoining Laboratory of the University of Waterloo, Ontario, Canada, was produced using the 0.7 μm CMOS process of AMIS, Oudenaarde, Belgium.

The CMOS test chip with the microsensor used in this work is shown in Fig. 1(a). The microsensor consists of an octagonal shaped bond pad with silicon resistors integrated adjacent to it as shown by the example in Fig. 1(b). These resistors are serpentine shaped and connected in a Wheatstone bridge configuration as shown in Fig. 2(a) and (b). The Wheatstone bridge is powered by a constant supply voltage V_s. The voltage across the bridge is calculated using $V_B = V_H - V_L$, where V_H is the voltage taken between R_1 and R_3, and V_L is the voltage taken between R_2 and R_4. The geometrical design of the sensor element is described in Section 3. The sensors operate on the piezoresistive principle: a change in applied force (or stress) causes a corresponding change in resistance of the piezoresistor.

The resistors are made from n^+ diffused silicon and are along the [0 1 0] crystal direction. These resistors sense the z-force indirectly by measuring the shear stress σ which extends outside the contact zone along the [0 1 0] axis [6]. The piezoresistance effect of silicon is described in [7]. The design and operation details of these sensors are similar to those described in [3].

The microsensor test chip is mounted on a 18-terminal side brazed dual-in-line (DIP) package using a commercial silver filled epoxy, and cured in an oven at 150 °C for 90 min. The connection pads to the sensors are electrically connected to the terminals by gold wire bonds. The chip-package assembly and the shielded cable are mechanically clamped by screws to the oven plate which is fixed to the wire bonder heater stage. The real-time, in situ signals from the microsensor during the bonding process are filtered and amplified using an operational amplifier and an external power supply

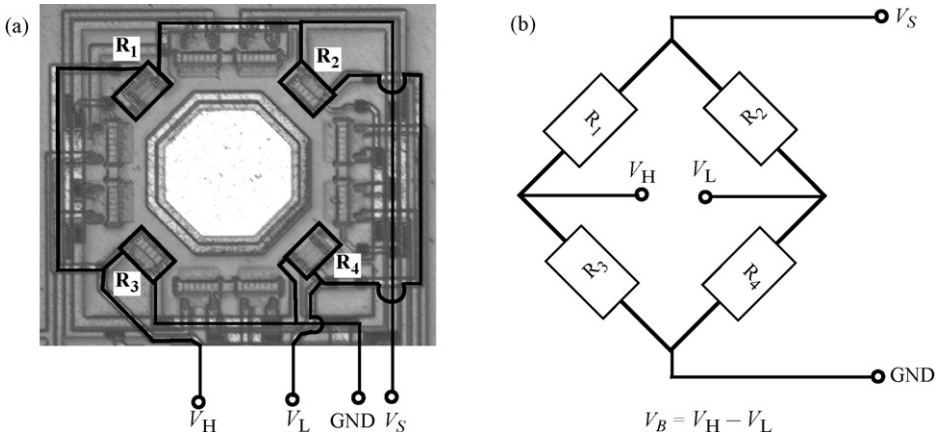

Fig. 2. (a) Identification of connections to microsensor elements next to test pad. (b) Electrical circuit diagram.

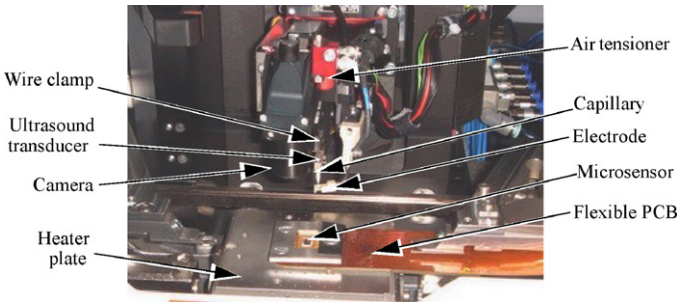

Fig. 3. Photograph of experimental setup on wire bonder.

Table 1
Bonding parameters for *z*-force sensor calibration experiments

Parameters	Values
Impact force	350 mN
Bond force	24–750 mN
Ultrasound power	0%
Bond time	10 ms
Bond temperature	25 °C
FAB diameter	50 μm

which are controlled using a custom made program on a PC. An overview of this setup is shown in Fig. 3.

2.1. Microsensor under compressive force

A method to calibrate the microsensor for *z*-force measurement using no-wire capillary tests (capillary imprint) is reported in [3]. In this method, the capillary tip is pressed directly on the test pad. The capillary tip is ring-shaped and exerts a higher pressure only at certain regions of contact with the microsensor bond pad.

As such, it has a less uniform contact with the test pad when compared to that of a deformed ball during an actual bonding situation. It is thought worthwhile to investigate how much the *z*-force sensitivity factor of the microsensor changes from the no-wire to the wire situation. Tests representing both situations are performed using the parameters given in Table 1. In both cases, the tests are repeated ten times. The capillary imprint test is performed in no-wire mode, and for the ball imprint tests ultrasound is not applied. Therefore, actual bonding on the microsensor is not taking place in both cases. Fig. 4 shows example signals of the capillary pressing on the microsensor bond pad with different values of bonding force. The microsensor force signal, S, is the ratio of change in V_B to $V_s = 3$ V: $S = V_B/V_s$. The higher frequency signal vibrations recorded during the first 2–3 ms are not observed if wire is used.

The *z*-force signal of the microsensor under compressive force, S_c, is evaluated as the average of the microsensor response between the two vertical lines indicated in Fig. 4, for each value of the nominal bonding force (F_c). Fig. 5(a) and (b) show a linear relationship between S_c and F_c for no-wire capillary imprint tests and for Au ball imprint tests, respectively. The slope of the linear fit is defined as the *z*-force sensitivity factor of the microsensor under compressive force, f_c.

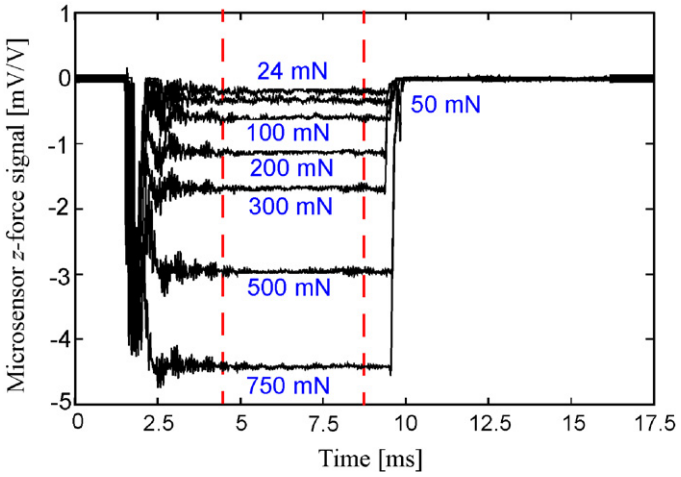

Fig. 4. Example signals from microsensor under different compressive forces exerted by capillary tip without wire.

It is observed that for the two largest values of the bonding force (i.e., 500 and 750 mN), the bonding force exceeds the impact force. These results in a ball of larger diameter imprinting on the bond pad when compared to the cases where bonding force was less than the impact force. Therefore, the largest two data values of Fig. 5(b) are removed and re-plotted in Fig. 5(c). The sensitivity factors f_c are determined from the plots in Fig. 5(a) and (c) and are 5.69 ± 0.09 and 4.95 ± 0.21 mV/V/N for the no-wire capillary tests and for Au ball tests, respectively. Each error term is the standard deviation of f_c and referred to as s in Section 3.4.

2.2. Microsensor under tensile force

The microsensor can be used for real-time, in situ measurement of tensile force, such as the TBF signal [3]. The range of *z*-tear speed available on the used wire bonder is 2–80 mm/s. As the length of the wire under tensile load is fixed at 15 mm, strain rates of 0.13–5.3 s^{-1} are possible.

To measure the tensile strength of the HAZ of the ball bond, the bonding process is modified by adjusting the values of the bonding parameters for ball and wedge bond to those shown in Table 2. During the ball bond process, the impact force of 500 mN causes the initial deformation of the FAB, but a low bond force combined with no ultrasound ensures that the deformed FAB does not stick to the dummy ball bond position defined on a location other

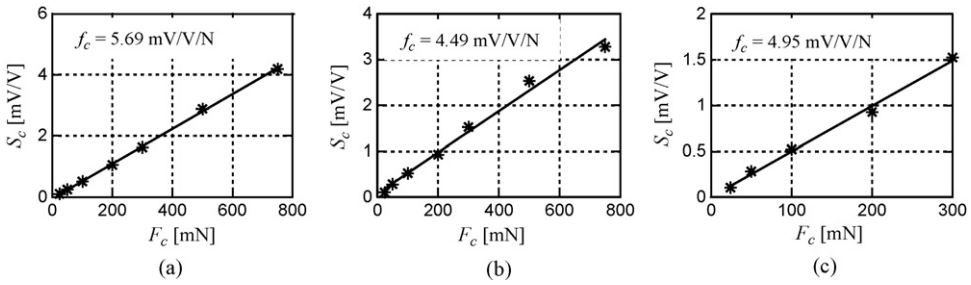

Fig. 5. S_c vs. F_c plots for (a) no-wire capillary imprint tests, (b) 50 μm diameter gold ball imprint tests, (c) 50 μm diameter gold ball imprint tests, re-calculated excluding the largest two bonding force values.

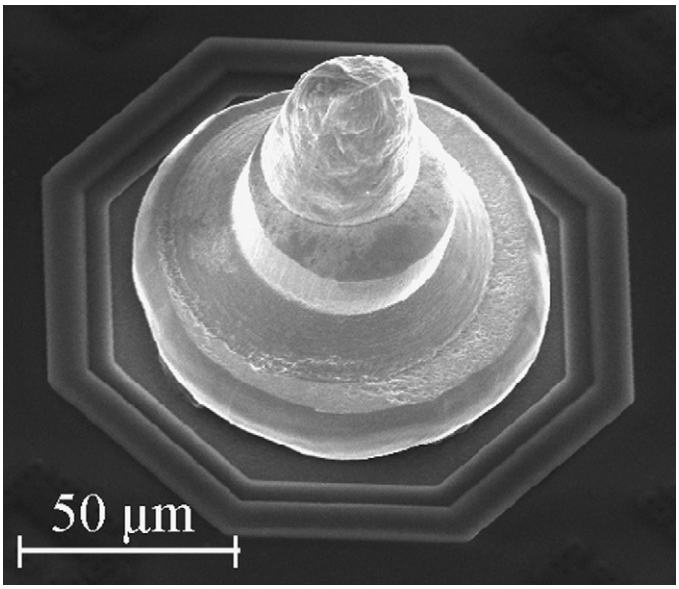

Fig. 6. SEM micrograph of ball bond on microsensor test pad with wire broken at HAZ.

than the microsensor pad. The non-stick detection option of the bonder is switched off, so the capillary continues on the looping trajectory. However, it does not form a loop but transports the ball which is stuck at the capillary tip, to the second bond location on the microsensor pad. During the second bonding process, the optimized ball bonding parameters are used so that the deformed ball is bonded on the test pad. During the subsequent tail formation process, the wire breaks at the HAZ. An SEM micrograph of the gold ball bond on the microsensor test pad after the wire broke at the HAZ is shown in Fig. 6.

Table 2
Bonding parameters for wire pull measurement experiment

Parameters	Ball bond	Wedge bond
Impact force	500 mN	600 mN
Bond force	50 mN	400 mN
Ultrasound power	0%	40%
Bond time	2 ms	30 ms
Bond temperature	25 °C	25 °C

The measurement is performed on ten samples and the real-time signals of the microsensor are recorded. The online signal of the complete test bond cycle is shown in Fig. 7(a). The signal with the wire under tensile force is shown in Fig. 7(b) exhibiting a sharp step on the occasion of wire breaking. The TBF value is measured as the height of the step. Its average is denoted S_t and is 0.169 mV/V. The standard deviation of S_t is 0.006 mV/V, indicating a signal precision of about 1%. To find the wire breaking force F_t, the sensitivity factor of the microsensor under tensile force $f_t = S_t/F_t$ is determined in the next section.

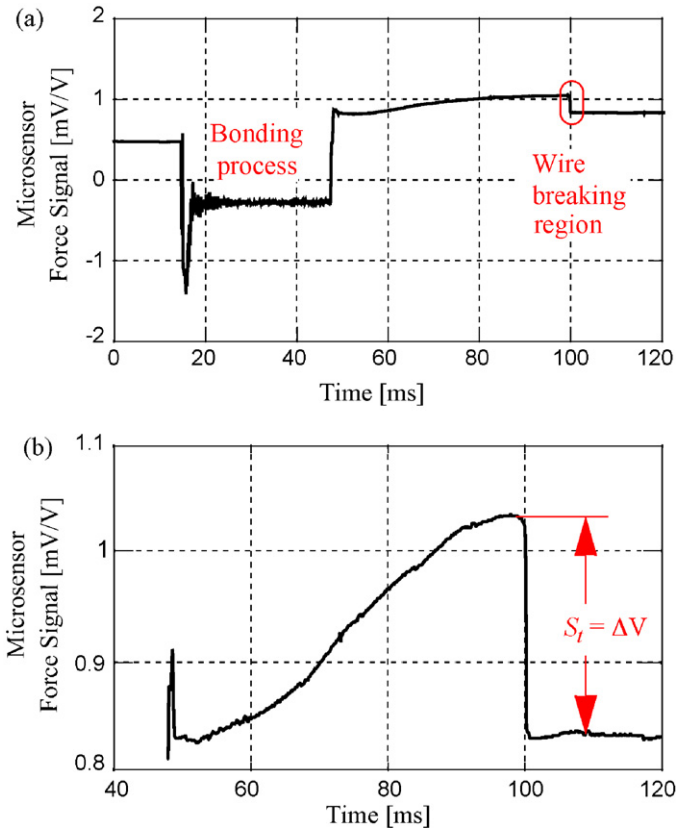

Fig. 7. Real-time, online signals of microsensor (a) during wedge bonding process, (b) example measurement of wire breaking force.

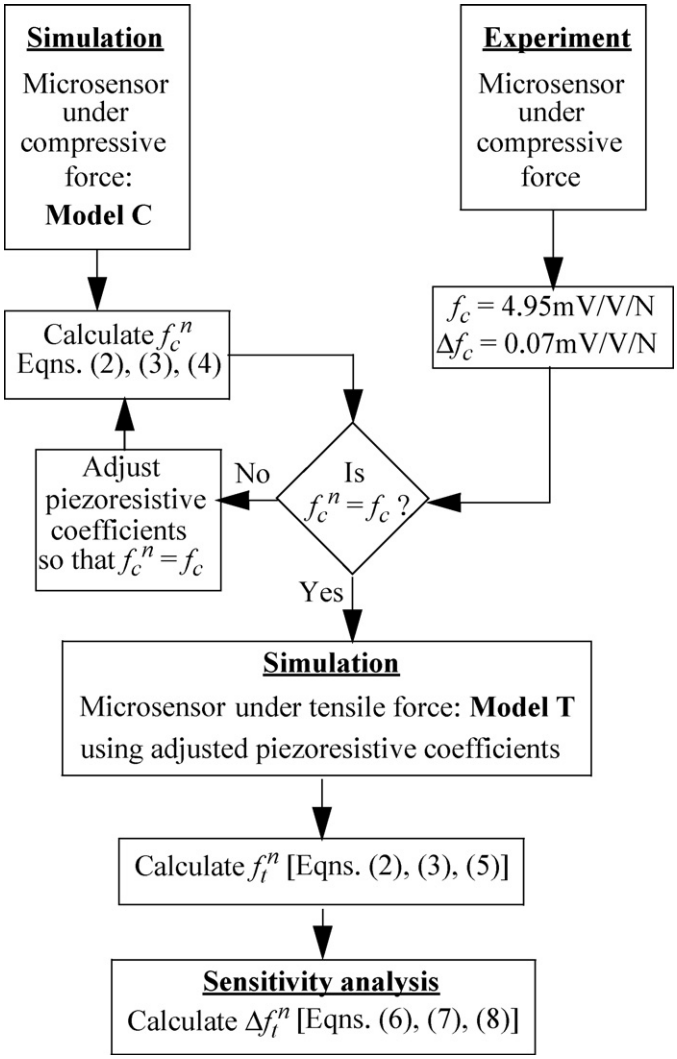

Fig. 8. Flowchart outlining procedure to calculate f_t^n, and Δf_t^n.

3. FE assisted analysis

Numerical FE modeling is used to compute the stresses under the bonding pad when subjected to compressive bonding force (Model C) and tensile wire pull (Model T) loading conditions. Using values for the piezoresistive coefficients and (Eq. (2)) given in Section 3.3, an equivalent for the microsensor signal can be derived from the simulation. The simulated microsensor response is used to compute the factor f_t and its error Δf_t as shown by the flowchart in Fig. 8. The piezoresistive coefficients are adjusted until the simulated microsensor signal matches the experiment in model C. The adjusted coefficients are used for model T.

3.1. FE models

3-D solid stress–strain models of the capillary pressing the ball on the bonding pad denoted Model C, and the wire pull at the ball neck denoted Model T are implemented in COMSOL Multiphysics Structural Mechanics Module, a commercial FE software. Table 3 lists the material properties used in the analyses. Anisotropic property of silicon is taken into account, with the elasticity matrix taken from the COMSOL materials library. All other material properties are taken from [6]. The meshed geometries of the two models are schematically shown in Fig. 9(a) and (b), respectively. Only a quarter of the geometry is modeled for symmetry reasons. The geometry details of both the models are essentially the same, except that the capillary tip is removed from model T. The parameterization of the model is shown in Fig. 10. For both models, stationary stress–strain analysis is performed using quadratic Lagrange elements. SPOOLES is selected as the linear system solver. A maximum mesh element size of 1 μm is selected for the bond pad which produces a total of 26,192 and 25,891 tetrahedral elements for Model C and T, respectively.

In Model C, a compressive force of $F_c^n = 750$ mN is applied to the capillary by defining a boundary condition of 94.8 MPa to the top plane of the capillary tip, while in Model T, a tensile force of $F_c^n = 50$ mN is applied to the wire by defining a boundary condition of 98.7 MPa to the top plane of the wire. In addition, the chip

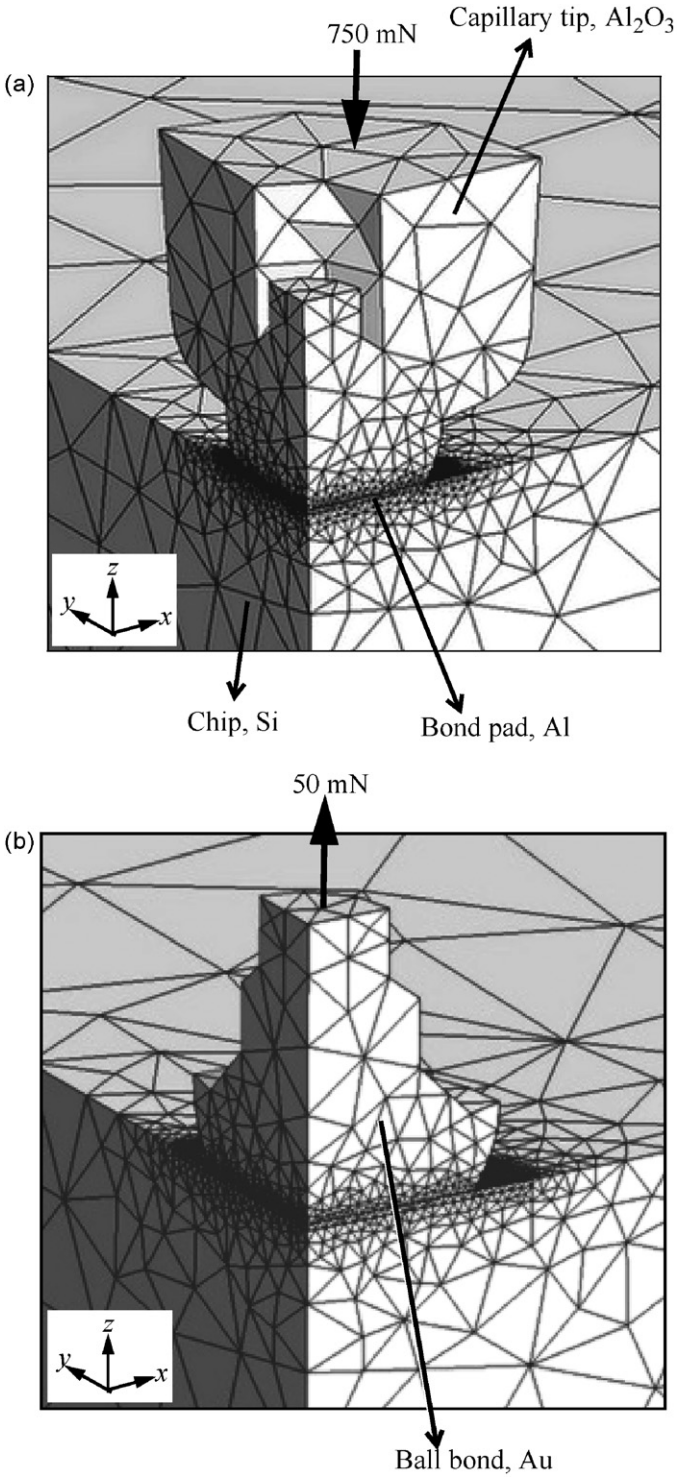

Fig. 9. FE models: (a) Model C and (b) Model T.

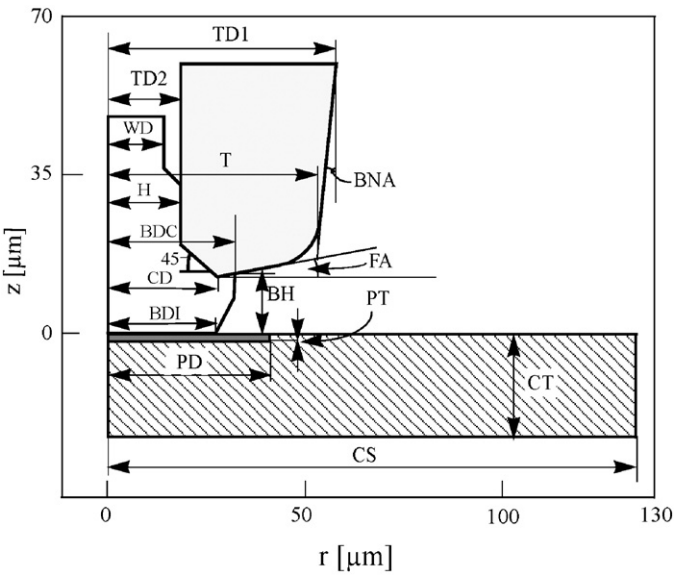

WD = 12.7 μm	T = 50 μm	CD = 25.5 μm
BH = 12 μm	TD1 = 53.1 μm	PD = 37.5 μm
BDI = 26 μm	TD2 = 17.5 μm	PT = 2 μm
BDC = 30 μm	BNA = 10°	CT = 500 μm
H = 17.5 μm	FA = 11°	
OR = 12 μm	CS = 125 μm	

Fig. 10. Parametric model of bonded ball, capillary, bond pad, and microsensor chip with parameter values.

Table 3
List of material properties

Part	Material	Elastic modulus [GPa]	Poisson's ratio
Capillary	Al_2O_3	410	0.25
Wire/ball	Au	77.2	0.424
Bond pad	Al	70	0.35
Test chip	Si	Elasticity matrix [10^{11} Pa]:	$\begin{bmatrix} 6.6 & 13.4 & 13.4 & 0 & 0 & 0 \\ 13.4 & 6.6 & 13.4 & 0 & 0 & 0 \\ 13.4 & 13.4 & 6.6 & 0 & 0 & 0 \\ 0 & 0 & 0 & 0.75 & 0 & 0 \\ 0 & 0 & 0 & 0 & 0.75 & 0 \\ 0 & 0 & 0 & 0 & 0 & 0.75 \end{bmatrix}$

bottom is constrained so it is not moving in the z-direction in both models. The following simplifications and assumptions are used in the analysis.

(1) All the CMOS layers are omitted except for the Al layer stack of the pad, the thickness of which is fixed at 2 μm.
(2) The microsensor is located between 48 and 64 μm from the centre of the bond pad along the [0 1 0] crystal direction (as shown in Fig. 11), and 2 μm below the chip surface.
(3) The interface is a perfect bond in both models, allowing no sliding in Model C, and no partially bonded areas in Model T.
(4) The material parameters are the same before and after bond formation.

3.2. FE stress distributions

The microsensor is located between 48 and 64 μm from the center of the bond pad along the [0 1 0] crystal direction, i.e., at 45° between the x- and the y-axis as shown by the layout in Fig. 11, and at a depth of 2 μm below the chip surface. The variation in normal and shear stresses along this line from the center of the bond pad is shown in Fig. 12. The microsensor is sensitive to the stresses experienced in the area defined by the rectangle $a \times a$ as illustrated in Fig. 11. For simplicity, it is assumed that the stress components averaged along the radial line inside the $a \times a$ area acceptably represents the average over the entire $a \times a$ area. Table 4 shows the averages and the standard deviations of the simulated normal and shear stresses at the sensor location along the radial line for both models.

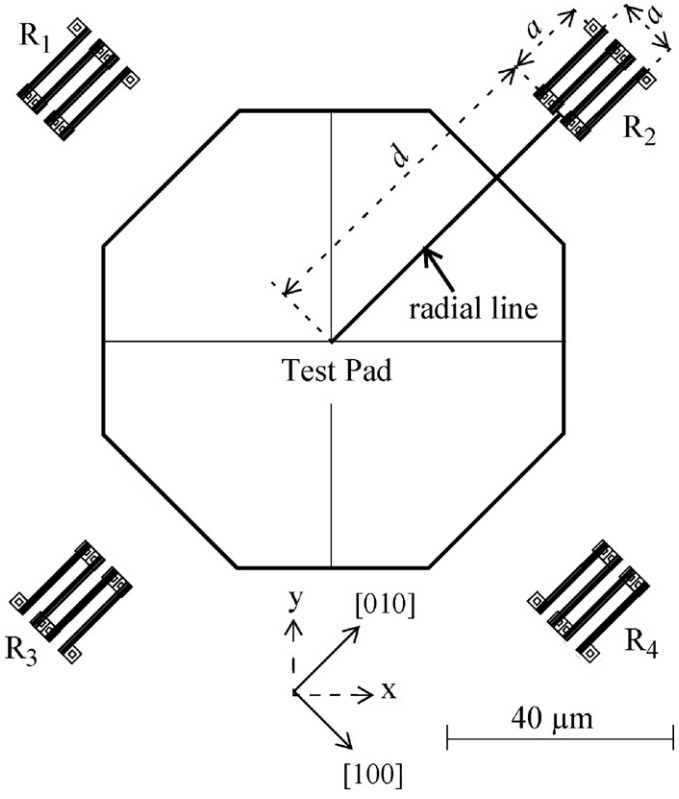

Fig. 11. Layout of microsensor elements next to test pad.

3.3. Piezoresistive response

The microsensor z-force sensor operates on the piezoresistive principle: when subjected to a mechanical stress change, the piezoresistive elements undergo a change in electrical resistance. A detailed description of the physics, mathematical description, and measured material properties of piezoresistance effect can be found in [6–8]. In the following, the expressions required to simulate the sensor response are excerpted. The symbols used in the expressions are defined below.

σ	mechanical stress
σ_{ii}	normal stress in i direction
τ_{ij}	shear stress in plane i and direction j
ΔR	change in resistance of the microsensor subjected to mechanical stress
R	nominal resistance of each of the microsensor elements
ϕ	angle between the current flow in the resistor and the x-axis
π_{11}, π_{12}	piezoresistive coefficients
S^n	microsensor signal obtained from simulation
F^n	applied force. Model C: $F_c^n = 0.75$ N and Model T: $F_t^n = 0.05$ N
f_c	sensitivity factor of the microsensor under compressive force, obtained from experiment
f_c^n	sensitivity factor of the microsensor under compressive force, obtained from simulation
f_t^n	sensitivity factor of the microsensor under tensile force, obtained from simulation
s_f	standard deviation of f_c
Δf_c	error of f_c
Δf_t^n	error of F_t^n

Table 4
Simulated stresses at sensor location

Stress component	Model C		Model T	
	Average [MPa]	S.D. [MPa]	Average [MPa]	S.D. [MPa]
xx	−3.38	1.37	0.40	0.14
yy	−3.20	1.33	0.43	0.12
zz	−0.09	0.54	−0.01	0.07
xy	7.59	0.83	−0.26	0.05
yz	0.36	0.50	−0.03	0.02
xz	0.34	0.32	−0.01	0.03

When the piezoresistive element is subjected to a mechanical stress given by the stress tensor in (Eq. (1)),

$$\sigma = \begin{bmatrix} \sigma_{xx} & \tau_{xy} & \tau_{xz} \\ \tau_{xy} & \sigma_{yy} & \tau_{yz} \\ \tau_{zx} & \tau_{zy} & \sigma_{zz} \end{bmatrix} \quad (1)$$

it undergoes a subsequent change in resistance given by (Eq. (2)):

$$\left.\frac{\Delta R}{R}\right|_{\phi=45^\circ} = \sigma_{xx}\left[\frac{\pi_{11}+\pi_{12}}{2}\right] + \sigma_{yy}\left[\frac{\pi_{11}+\pi_{12}}{2}\right] + \sigma_{zz}\pi_{12} + \tau_{xy}[\pi_{11}+\pi_{12}] \quad (2)$$

where π_{11} and π_{12} are the piezoresistive coefficients of the n^+ material. Values of π_{11} and π_{12} found in [9,10] range from -3.68 to -4.3×10^{-10}, and 1.90 to 2.42×10^{-10} Pa^{-1}, respectively.

The four piezoresistive elements are arranged in a full Wheatstone bridge configuration. Therefore, the change in normalized resistance given by (Eq. (2)) is equal to the change in normalized Wheatstone bridge voltage. Thus, the microsensor signal is given by (Eq. (3)).

$$S^n = \frac{\Delta V}{V} = \frac{\Delta R}{R} \quad (3)$$

The sensitivity factors of the microsensor are defined as the relative resistance change divided by the applied force. For the compressive and the tensile cases, this relationship is given by (Eqs. (4) and (5)), respectively.

$$f_c^n = \frac{S_c^n}{F_c^n} = \frac{S_c^n}{0.75} \quad (4)$$

$$f_t^n = \frac{S_t^n}{F_t^n} = \frac{S_t^n}{0.05} \quad (5)$$

In order to match the simulated value f_c^n with the experimental value f_c, the values of π_{11} and π_{12} are adjusted. A contour plot of f_c^n as a function of π_{11} and π_{12} is shown in Fig. 13. For successful matching, any point lying on the contour line $f_c^n = 4.95$ mN/V/N can be selected. The values $\pi_{11} = 3.68 \times 10^{-10}$ and $\pi_{12} = 1.97 \times 10^{-10}$ Pa^{-1} are selected to evaluate f_t^n as they are approximately in the middle of the contour line. For these values, the factors f_c^n and f_t^n are calculated to be 4.95 and 1.54 mV/V/N, respectively.

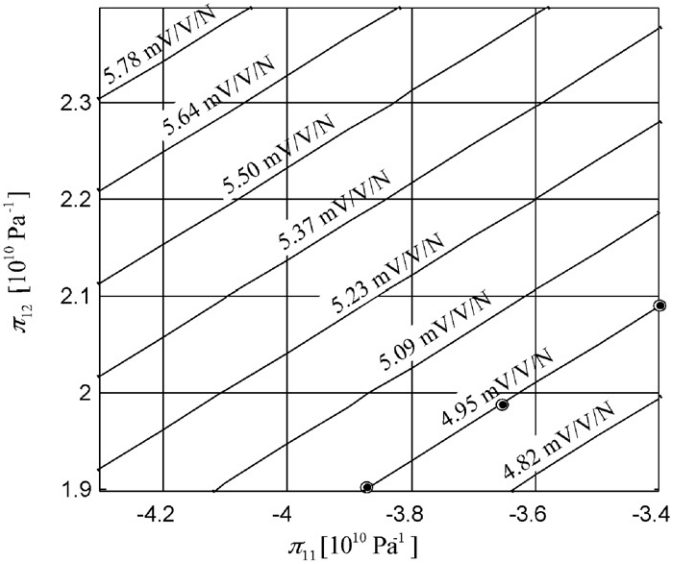

Fig. 13. Contour plot f_t^n as function of π_{11} and π_{12}.

3.4. Sensitivity analysis

Table 5 shows the average change in the values of f^n for models C and T for the estimated variation in the values of various parameters. The error estimate is the assumed or expected variation for these parameters except for ball placement and geometry. In the case of ball placement (BP), ball diameter (BDC), and ball height (BH), these values are measured using an optical microscope and the error estimate is calculated as the error of the average using (Eq. (6)).

$$\Delta = \frac{s}{\sqrt{n-1}} \quad (6)$$

where Δ s, and n are error, standard deviation, and sample size, respectively.

It is observed that the microsensor signal is highly sensitive to variations in π_{11} and π_{12}, pad thickness, z-location of the sensor

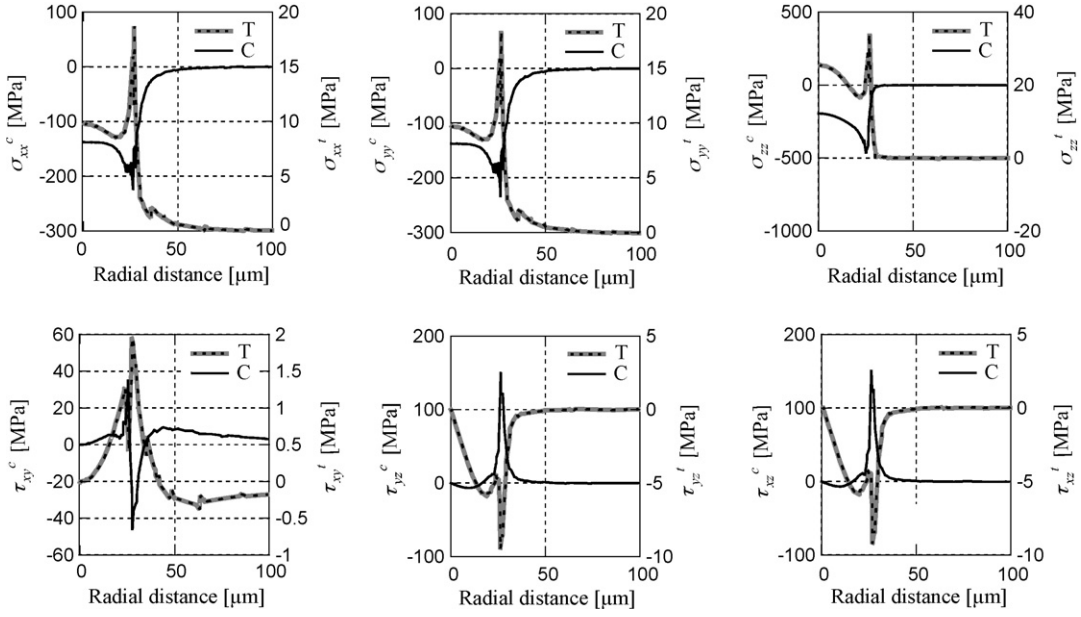

Fig. 12. Simulated stress distributions along the radial distance 45° between the x- and y-axis and 2 μm below the chip surface for model C, and model T.

Table 5
Sensitivity analysis

Parameters				Model C		Model T	
Group	Name	Error estimate		Δf_c^n	Δf_c^n	Δf_t^n	Δf_t^n
		Type	Value	[mV/V/N]	[%]	[mV/V/N]	[%]
Model	Mesh (ΔM)	Variation (assumed)	Min. size 1–2 μm	−0.03	−0.57	−0.09	−6.09
Sensor location	Δz	Error (assumed)	0.25 μm	0.36	7.29	0.35	22.6
	Ball placement (ΔBP)	Error of average	0.2 μm	0.04	0.76	0.02	1.26
Ball and pad geometry	ΔBDC	Error of average	0.2 μm	0.03	0.69	0.02	1.39
	ΔBH	Error of average	0.2 μm	−0.04	−0.75	−0.03	1.92
	ΔPT	Error (assumed)	1 μm	−0.24	−4.89	−0.45	−29.0
Material Young's moduli	Wire (ΔW)	Error (assumed)	10 GPa	−0.002	−0.04	−0.08	−5.49
	Pad (ΔP)	Error (assumed)	10 GPa	0.06	1.30	0.16	10.6
Piezo coefficients	π_{11}, π_{12} ($\Delta\pi$)	Variation [9,10]	$(\pi_{11}, \pi_{12}) = (-3.87, 1.9)$ to $(-3.44, 2.07)$ in Fig. 13	0	0.00	−0.36	−23.2
Total error				0.44	8.93	0.70	45.8

under the bond pad, elastic modulus of pad and wire, mesh size, ball geometry and placement. Furthermore, it is observed that ±5% changes in the Poisson's ratio of the materials, and variations in elastic modulus of capillary in Model C have negligible effects on the result. Errors of the elasticity matrix of the Si chip are assumed to be negligible.

The error Δf^n is calculated using (Eq. (7)) which is based on the theory of combination of component errors in overall system accuracy calculations [11]. For model T, the value of Δf_t^n is found to be 0.70, which is approximately 46% of f_t^n.

$$\Delta f^n = \sqrt{\Delta M^2 + \Delta z^2 + \Delta \mathrm{BP}^2 + \ldots + \Delta \pi^2} \quad (7)$$

Variation in π_{11} and π_{12} along the contour line $f_c = 4.95$ mV/V/N (Fig. 13) results in an error of about 23.2% (Table 5). Thus, the accuracy of f_t^n can be improved if exact values of π_{11} and π_{12} can be found. Additional sensing elements made from the same material could be designed to improve the accuracy of the determination of the piezoresistive coefficients. However, this is not carried out in this work due to the availability of an alternative method discussed in the next section.

4. Proximity sensor

A proximity sensor is attached to the wire clamp of the wire bonder as shown in Fig. 14. The proximity sensor is a displacement sensor which works on the eddy current principle to sense the proximity of conductive materials. The main benefits of such a sensor are non-contacting measurement, high frequency response, and high resolution. The displacement measured is the change of gap between the sensor and the ultrasonic transducer and is proportional to the force acting on the horn. Normally, it is calibrated to give online signals of the actual bonding force applied by the horn during the bonding process. In this study, it is used to measure the wire breaking force exerted by the clamp. The calibration factor f_P and its error Δf_P are determined first.

The tensile force signal of the proximity sensor is calibrated directly by hanging a known weight of 22.2 g to the wire clamp, as shown in Fig. 15, resulting in a force of 218 mN acting vertically

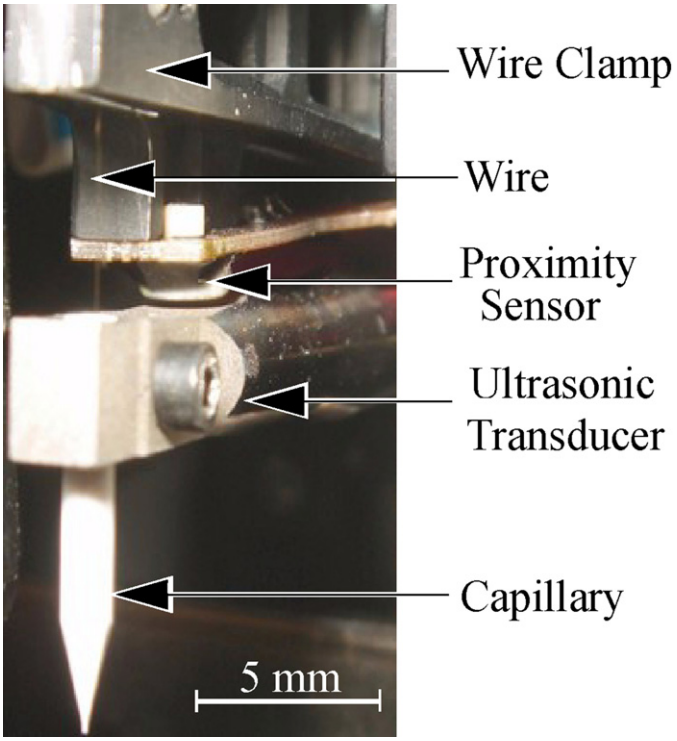

Fig. 14. Proximity sensor, wire clamp, and ultrasonic transducer.

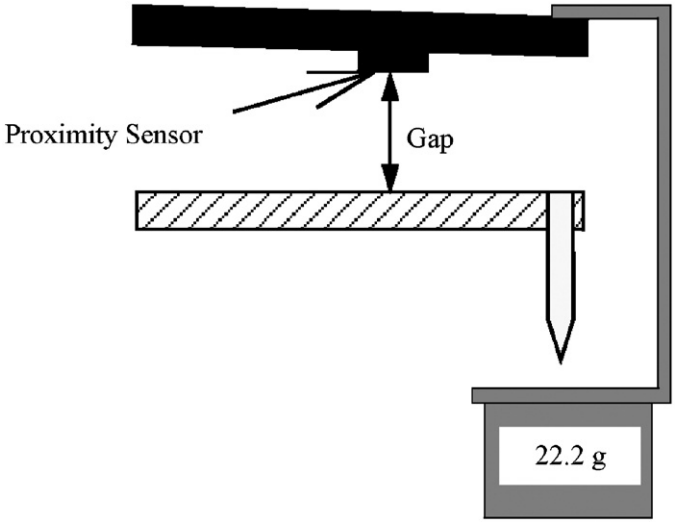

Fig. 15. Schematic illustration of a 22.2 g weight hanging freely on the wire clamp.

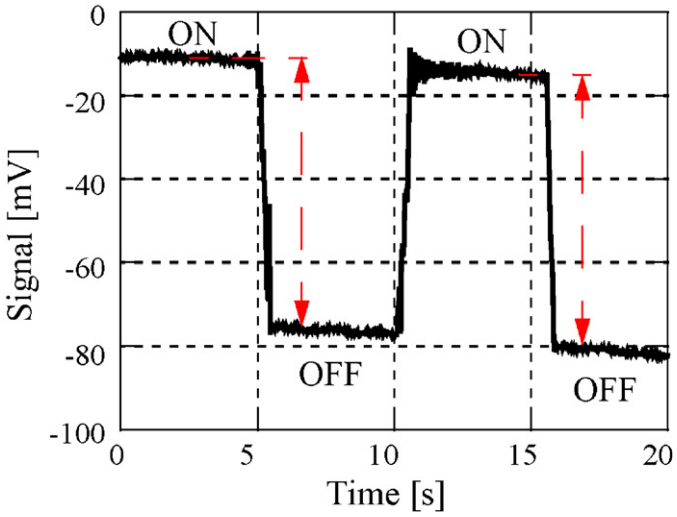

Fig. 16. Proximity signal of a 22.2 g weight hanging freely on the wire clamp and being removed twice.

downwards. The signal shown in Fig. 16 is recorded on an oscilloscope while the weight is hung (ON) and removed (OFF) twice. This method requires the extraction of the signals when the wire bonder is in idle state. Special tools and support from the wire

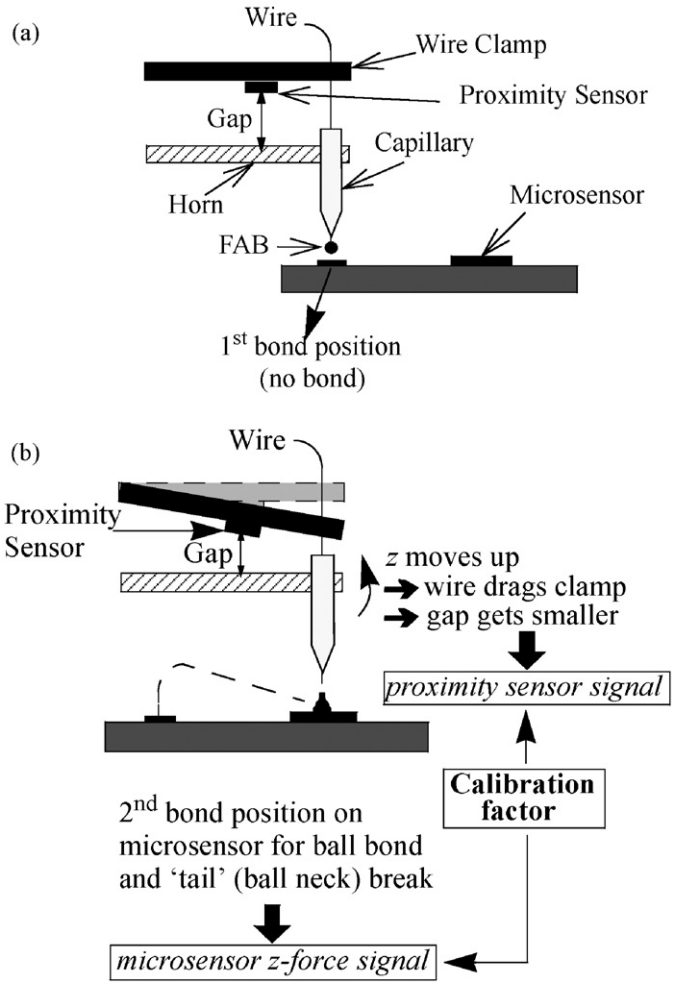

Fig. 17. Schematic illustration of modified bonding process. (a) Situation prior to first bond, (b) situation during wire break.

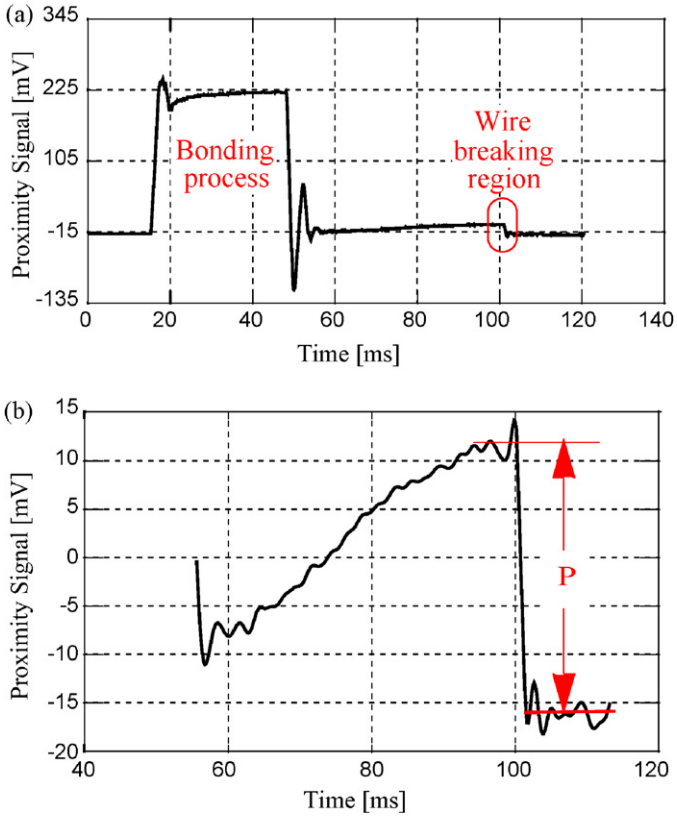

Fig. 18. Real-time, online signals of proximity sensor (a) during wedge bonding process, (b) example measurement of wire breaking force.

bonder manufacturer are required for the signal extraction. The signal drop of the proximity sensor upon removal of the weight is 63.2 ± 2.12 mV. From this value, the calibration factor, f_P is computed to be 290 ± 10 mV/N.

4.1. Wire breaking force

While bonding a ball on the microsensor test pad using the modified bonding process and subsequently breaking the wire as illustrated in Fig. 17(a) and (b), the microsensor force signal and the proximity sensor signal are recorded simultaneously. The experiment is repeated ten times, each time a new microsensor test chip is used. Example microsensor and proximity sensor signals are shown in Figs. 7(a) and 18(a), respectively. Examples of the corresponding wire breaking signal portions are shown in Figs. 7(b) and 18(b), respectively. The average proximity sensor signal is $P = 28.6$ mV, respectively. The standard deviation of the signal is 0.85 mV, indicating a signal precision of 1% for the proximity sensor.

The average wire breaking force F_t is the ratio of P and f_P. The error of F_t denoted ΔF_t is calculated using (Eq. (8)).

$$\Delta F_t = \sqrt{\left(\frac{\Delta P}{f_P}\right)^2 + \left(\frac{\Delta f_P \cdot P}{(f_P)^2}\right)^2} \tag{8}$$

Using $f_P = 290 \pm 10$ mV/N, the average wire breaking force $F_t \pm \Delta F_t$ is calculated to be 98.6 ± 1.67 mN. This value is approximately 77% of the nominal tensile strength of the wire which is measured using a standard micro-tensile testing machine to be 128 mN.

The microsensor is calibrated again, this time by the proximity sensor using (Eqs. (9) and (10)):

$$f_t = \frac{S_t}{F_t} \tag{9}$$

$$\Delta f_t = \sqrt{\left(\frac{\Delta S_t}{F_t}\right)^2 + \left(\frac{\Delta F_t \cdot S_t}{F_t^2}\right)^2} \tag{10}$$

where S_t is the microsensor signal and ΔS_t is the error of S_t.

The calibration factor of the microsensor $f_t \pm \Delta f_t = 1.71 \pm 0.03$ mV/V/N. This value is within the range found previously using the FE analysis and has a smaller error.

5. Concluding remarks

Automatic, online methods to measure the wire breaking force with a commercial wire bonder using an integrated microsensor and a proximity sensor are reported. Both these methods are fast, highly sensitive, precise and robust. The microsensor method uses a special test chip with integrated piezoresistive microsensor. Due to a bandwidth of several MHz together with a fast measurement system, the wire breaking force can be measured even at higher strain rates up to 5.33 s using this method. The advantage of the proximity sensor method is the automatic measurement by the wire bonder with no necessity of specially designed test chips. However, due to the constraints of the electronics available, this method is currently limited to measure the wire breaking force at low strain rates to avoid significant accuracy loss. An application of these methods is to quantify relative TBF variations automatically in real-time and under in situ conditions. The methods can be used to study the breaking strength of the HAZ of the ball bond. For absolutely accurate results, the force signals need to be calibrated.

Acknowledgements

This work is supported in part by Ontario Centres of Excellence (OCE), Natural Sciences and Engineering Research Council of Canada (NSERC), Microbonds Inc. (Markham, Ontario, Canada), and MK Electron. Co. Ltd. (Yongin, South Korea). Technical help of Oerlikon Esec (Cham, Switzerland) is gratefully acknowledged.

References

[1] G. Harman, Wire Bonding in Microelectronics: Materials, Processes, Reliability and Yield, second ed., McGraw-Hill, New York, 1997.
[2] D.R.M. Calpito, D.T. Alcala, Tail lift-off solution for fine pitch applications, in: Proceedings of SEMICON 2004, Singapore, 2004, pp. 1–5.
[3] J. Schwizer, M. Mayer, O. Brand, Force Sensors for Microelectronic Packaging Applications, Springer, Berlin, 2005.
[4] J. Lee, M. Mayer, Y. Zhou, S.J. Hong, S.M. Lee, Tail breaking force in thermosonic wire bonding with novel bonding wires, in: Proceedings of International Welding and Joining Conference, 2007.
[5] J. Lee, M. Mayer, Y. Zhou, Iterative optimization of tail breaking force of 1 mil wire thermosonic ball bonding processes and the influence of plasma cleaning, Microelectronics Journal 38 (2007) 842–847.
[6] M. Mayer, Microelectronic Bonding Process Monitoring by Integrated Sensors, Ph.D. Dissertation ETH No. 13685, Physical Electronics Laboratory, ETH Zurich, Switzerland, 2000.
[7] Y. Kanda, Piezoresistance effect of silicon, Sensors and Actuators A 28 (1991) 83–91.
[8] D.A. Bittle, J.C. Suhling, R.E. Beaty, R.C. Jaeger, R.W. Johnson, Piezoresistive stress sensors for structural analysis of electronic packages, Journal of Electronic Packaging 113 (1991) 203–215.
[9] J.N. Sweet, Die stress measurement using piezoresistive stress sensors, in: Thermal Stress and Strain in Microelectronics Packaging, Van Nostrand Reinhold, New York, 1993, pp. 221–271.
[10] M. Mayer, O. Paul, H. Baltes, Complete set of piezoresistive coefficients of CMOS n^+-diffusion, Journal of Micromechanics and Microengineering 8 (1998) 158–160.
[11] E.O. Doebelin, Measurement Systems Application and Design, fourth ed., McCraw-Hill, New York, 1990, pp. 58–67.

Biographies

Aashish S. Shah received his BTech in 2002 from Jawaharlal Nehru Technological University, Hyderabad, India and MASc in 2006 from the University of Ottawa, Ontario, Canada. He is currently pursuing his PhD in the Department of Mechanical and Mechatronics Engineering at the University of Waterloo, Ontario, Canada. His current research interest is process and bonding mechanism in microelectronic wire bonding process using integrated CMOS microsensors. Currently, he is working towards developing novel low-stress copper ball bonding processes, which minimize the risk of damage to the silicon chip.

Jaesik Lee received his BASc and MASc degrees in Material Science and Engineering from the University of Seoul, Korea, and the PhD in Mechanical Engineering in 2008 from the University of Waterloo, Ontario, Canada. His research interests include studying and improving the wire bonding process and aims on finding solution how to increase the wire bond strength and long-term reliability.

Michael Mayer received his diploma degree in Physics in 1994 and PhD degree in Technical Sciences in 2000, both from ETH Zurich, Switzerland, developing a novel family of CMOS microsensors for real-time feedback during the thermosonic ball bonding process. For his thesis, he was awarded the ETH Medal in 2001. From 2000 to 2004, he was a senior R&D engineer with Esec, Cham, Switzerland. Michael co-authored more than 60 technical publications including patent applications, a book and several book chapters, journal and conference papers. Michael joined the faculty of the University of Waterloo, Ontario, Canada, in 2004.

Y. Norman Zhou received his BASc and MASc from the Department of Mechanical Engineering, Tsinghua University, Beijing, China and PhD from the Department of Metallurgy and Materials Science, University of Toronto, Toronto, Canada. He worked as a Lecturer at the Department of Mechanical Engineering, Tsinghua University and as a Materials Scientist at the Fuel Development Branch, Atomic Energy of Canada, Ltd, Chalk River, Ontario, Canada. He also worked as a Senior Research Engineer at the Microjoining and Plastics Group at the Edison Welding Institute, Columbus, Ohio, USA. Dr. Zhou, currently a holder of Canada Research Chair in Microjoining (www.chairs.gc.ca), is also Professor at the Department of Mechanical and Mechatronics Engineering, University of Waterloo (www.mme.uwaterloo.ca). He has more than 20 years industrial, teaching and research experience in materials joining technologies. His current research interests include the field of microjoining and nanojoining (wire bonding, resistance and laser microwelding, brazing and soldering, etc.).